ADVANCED FUNCTIONAL MATERIALS
www.afm-journal.de

Soft and Stiff 3D Microstructures by Step-Growth Photopolymerization Using a Single Photoresin and Multi-Photon Laser Printing

Tugce Nur Eren, Jiajie Liang, Jonathan Ludwig Günter Schneider, Martin Wegener, Jens Bauer, Katharina Ehrmann,* Florian Feist,* and Christopher Barner-Kowollik**

Manufacturing three-dimensional (3D) microstructures with multi-material properties via two-photon 3D laser printing (2PLP) remains a significant challenge due to restrictions inherent to conventional chain-growth photoresins. Herein, an additive- and initiator-free resin formulation is introduced that allows for the printing of 3D microstructures with disparate mechanical properties via the step-growth photopolymerization-based self-dimerization of visible-light-active *ortho*-methylbenzaldehydes (*o*MBA) within a single fabrication step in 2PLP by altering the printing parameters (i.e., laser power, scan speed). It is established that the laser exposure dose (D_{exp}) directly influences the material properties by varying the degree of crosslinking. While stiff materials with a Young's modulus above 1300 MPa at the higher edge of the D_{exp} can be produced, soft materials with a Young's modulus of < 10 MPa at the lower edge of the D_{exp} can also be fabricated. Thus, the herein pioneered resin offers a very broad material property window – spanning more than two orders of magnitude in Young's modulus – for multi-material printing via 2PLP, which is not achievable with conventional resins. The capabilities of the advanced resin are demonstrated by printing structures with hard and soft segments in a single fabrication step, visualizing their unique mechanical response to compression via in situ measurements.

1. Introduction

Multi-photon 3D laser printing, or direct laser writing (DLW), of which two-photon 3D laser printing (2PLP) is a subset, is a photopolymerization-based additive manufacturing technique, which enables the fabrication of 3D structures at the nano- and micrometer scale.[1] This technique typically utilizes a femtosecond pulsed near infrared laser with a tight focus within a very small volume element (voxel) of a photosensitive monomer mixture (resin), allowing the production of highly spatially resolved 3D microstructures.[2] Smallest voxel dimensions reported for the above 3D printing method are below 100 nm, and typical widths and heights are ≥200 and ≥600 nm.[2b,3] The high intensity in the laser focal point allows the delivery of two photons sufficiently fast to excite the chromophore-containing molecule into its excited state with low-energy IR light (**Figure 1**). Thus, 3D laser printing

---

T. N. Eren, J. Liang, M. Wegener, J. Bauer, F. Feist, C. Barner-Kowollik
Institute of Nanotechnology (INT)
Karlsruhe Institute of Technology (KIT)
Hermann-von-Helmholtz-Platz 1, 76344 Eggenstein-Leopoldshafen, Germany
E-mail: jens.bauer@kit.edu; florian.feist@kit.edu; christopher.barner-kowollik@kit.edu

K. Ehrmann
Institute for Applied Synthetic Chemistry
Technische Universität Wien
Vienna 1060, Austria
E-mail: katharina.ehrmann@tuwien.ac.at

The ORCID identification number(s) for the author(s) of this article can be found under https://doi.org/10.1002/adfm.202502876

DOI: 10.1002/adfm.202502876

J. L. G. Schneider, M. Wegener
Institute of Applied Physics
Karlsruhe Institute of Technology (KIT)
Wolfgang-Gaede-Straße 1, 76128 Karlsruhe, Germany

J. Bauer
Institute for Applied Materials (IAM)
Karlsruhe Institute of Technology (KIT)
Kaiserstrasse 12, 76131 Karlsruhe, Germany

C. Barner-Kowollik
School of Chemistry and Physics
Centre for Materials Science
Queensland University of Technology (QUT)
2 George Street, Brisbane, QLD 4000, Australia

C. Barner-Kowollik
Institute for Functional Interfaces (IFG)
Karlsruhe Institute of Technology (KIT)
Hermann-von-Helmholtz-Platz 1, 76344 Eggenstein-Leopoldshafen, Germany

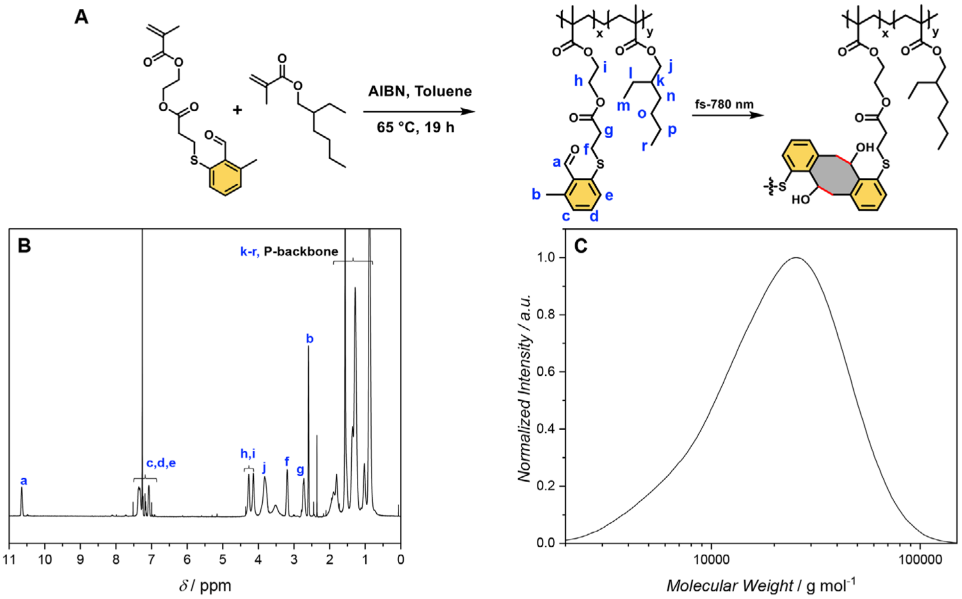

Figure 1. A) Synthesis of the polymer containing *o*-methyl benzaldehyde (*o*MBA) pendant units via conventional free-radical polymerization and its crosslinking mechanism during 3D printing. B) ^{1}H-NMR spectrum of poly(PEMA-*co*-EHMA) ($CDCl_3$, 400 MHz). C) SEC refractive index trace of poly(PEMA-*co*-EHMA) in THF (M_n = 15 400 g mol^{-1}, Đ = 1.7, x = 14, y = 56). Molecular weight calibration was conducted via PMMA standards. For further information, refer to Section 1.3.2 (Supporting Information).

has already been implemented in many different fields, e.g., microelectronics,[4] microrobotics,[5] microfluidics,[6] cell biology[7] and photonics.[1b,8] However, with few notable exceptions,[9] the majority of these applications still employ a homogeneous material composition throughout the printed objects, which significantly limits the design space. Therefore, multi-material 3D printing has become a major focus for resin design, where the material properties can be controlled as a function of the photocuring conditions during 3D printing.

While there have been significant efforts to use different colors of light to influence the material properties,[10] so-called gray-tone printing is an alternative viable approach for multi-material 3D printing. Gray-tone lithography, in which various material properties can be obtained depending on the printing conditions, is a common technique leveraged to generate graded or multi-property 3D microstructures.[9b,11] For instance, utilization of different printing parameters (i.e., laser power and scan speed) can transfer disparate mechanical properties to a single 3D microstructure by inducing local changes in the degree of crosslinking. Even though there are reports in the literature that address tuning the mechanical properties by adjusting the printing parameters,[12] the reported changes in Young's Moduli are not large, unless a post-processing step is carried out, or in specific cases such as hydrogels, which are significantly softer overall.[9b,13] Specifically, the fabrication of very soft high-resolution structures remains an unmet challenge, promising especially high reward for biofabrication applications. In the current contribution, we meet this challenge by introducing an advanced photoresin system capable of producing micro-printed objects with vastly differing material properties.

The difficulty in regulating the mechanical properties by changing the printing parameters stems from the nature of typically utilized radical chain-growth polymerization (CGP). In CGP, one photoinitiator molecule – activated through two-photon absorption – cures the photopolymer formulation by amplifying the quantum yield of the initial initiator decomposition via chain propagation (quantum yield, defined as the number of photochemical events that occur per photon of light absorbed),[14] leading to gelation at low monomer conversion, after which the reaction propagation becomes more diffusion-controlled. As a result, a non-uniform network forms, composed of inhomogeneously distributed crosslinks (creating regions of varying crosslinking density), linear polymer chains, chain cyclization, and dangling chain ends.[15] The aforementioned characteristics of CGP weaken the control of light dose over the degree of crosslinking and network uniformity, which dictates the overall mechanical properties.[16] To achieve efficient polymerization and crosslinking in each voxel during the 3D laser printing process, high concentrations of multifunctional monomers (crosslinkers) are typically used in resin formulations, which results in the generation of rigid structures due to high crosslinking densities. If the spacer between the functional groups of a crosslinker is designed to be more hydrophilic or flexible, soft materials can also be obtained, e.g., hydrogels[9b,17] or elastomers like polydimethylsiloxane (PDMS).[18]

Exploiting a different type of photopolymerization, such as step-growth photopolymerization (SGP), can provide better control over the material properties.[19] SGP has a very different conversion profile than CGP. In SGP, the crosslinked network is constructed slowly in a stepwise manner by repetitive occurrence of AA reactions (dimerization) between identical monomers, or AA/BB or AB reactions between separate monomers with two or more A and/or B functionalities. Consequently, gelation is only achieved at high conversion. Thus, the inhomogeneity of the formed network can only arise from chain cyclization or dangling chain ends, making it a more uniform network compared to the ones derived from CGP.[20] Photocycloaddition reactions, such as Diels-Alder, photodimerization or tetrazol-ene reactions, constitute an efficient SGP technique for designing materials with tunable properties by modifying printing parameters,[21] as each photoreactive functional unit must be activated individually by two photon absorption to participate in one of the aforementioned AA, AB or AA/BB type photoreactions, contrary to CGP, where one activated photoinitiator molecule already triggers formation of many different photoreactions.[16e,22] Thus, SGP chemistry enables precise control over the crosslinking density of the network, and thus the mechanical properties are readily adaptable by regulating the photon flux.[16f] In addition, photocycloaddition reactions, particularly those mentioned above, do not require a photoinitiator, which may cause cytotoxicity and color instability issues of the end product by leaching from the cured polymer produced by CGP.[23] It is important to note that copper catalyzed azide-alkyne cycloaddition (photo-CuAAC) reactions are an exception to the aforementioned mechanism of photocycloaddition reactions since they require an additional catalyst and a photoinitiator.

A photocycloaddition-based network formation can be achieved without a photoinitiator either through photodimerization of identical monomers containing a photoreactive unit (AA) or through the reaction between separate monomers containing different photoreactive units (AB, AA/BB). A wide variety of monomer choices in different combinations are available for photocycloaddition reactions, including multifunctional monomers, dilinkers containing photoreactive endgroups, and prepolymers containing multiple pendant photoreactive units per chain.[10] The use of a single (AA, AB) or two different prepolymers (AA/BB) containing pendant photoreactive moieties without any additional crosslinker can even provide a superior level of control over the material properties compared to other types of resin formulations, since each photoreaction forms one crosslink, resulting in network formation already at very low conversion. Additionally, stoichiometry and local monomer distribution do not influence polymerization efficiency. This resin design is uniquely suitable for fast and low power writing conditions for PDMS-like soft materials because only few crosslinking events are necessary to obtain form-stable networks from a prepolymer-only containing resin of already high molecular weight. Since the prepolymer resins require fewer bond forming events to establish a stable network, they can also be useful to remediate the issue of heat accumulation arising from highly intense two-photon absorption processes during the formation of a network with high crosslinking density. Additionally, higher viscosity compared to small molecular weight monomers restricts diffusion, enabling access to slower printing speeds without loss of spatiotemporal control. In addition, a prepolymer resin does not contain any small molecules or oligomers that could be extracted or leached during the life cycle of a printed structure.

Thus, employing photoresins based on prepolymers broadens the writing window for the fabrication of 3D structures, thereby expanding the array of different mechanical properties accessible from the resin. However, so far, prepolymers have only been used in combination with a crosslinker in a resin formulation for 3D laser printing applications, where crosslinking only occurs upon full consumption of the crosslinker, i.e., two photoreactions.[11b,24] Single and dual prepolymer approaches without any additional crosslinkers have previously been utilized by our group for the synthesis of precisely controlled microspheres.[25]

Herein, an additive- and photoinitiator-free resin formulation solely consisting of a prepolymer featuring pendant *ortho*-methyl benzaldehyde (*o*MBA) units is introduced to fabricate 3D microstructures with diverse mechanical properties via the self-dimerization of visible light active *o*MBA units, employing a commercially available 3D laser printing technology (**Scheme** 1A).[26] Since the crosslinking density of the formed network can be controlled with high precision by adapting the printing parameters (i.e., laser power, scan speed), a wide range of material properties from "soft" and PDMS-like to "stiff" can be achieved from a single resin within one fabrication process based on the unique design of our photoresin (Scheme 1B). We thus pave the way for achieving multi-material properties from a single photoresin by fine-tuning the mechanical properties through careful adjustment of the printing parameters, with high relevance for biological applications, microfluidics, or soft robotics.

2. Results and Discussion

2.1. Synthesis and Characterization of the Resin

For the resin preparation, the prepolymer poly(PEMA-*co*-EHMA) was synthesized by the copolymerization of an *o*-methyl benzaldehyde (*o*MBA) functionalized methacrylate and 2-ethylhexyl methacrylate (EHMA) via conventional free radical polymerization using 2,2′-azobis(2-methylpropionitrile) (AIBN) as a thermal initiator and dodecane thiol as chain transfer agent, which controls the number average molecular weight ($\bar{M}_n$) of the prepolymer (Figure 1A).[27] The prepolymer is the sole constituent of the resin in addition to the solvent used in minimum amounts (20 wt% acetophenone), since the crosslinking mechanism is based on the photodimerization of photoenolized *o*MBA units (Figure 1A, refer to Section 2.1, Supporting Information).[25] Therefore, the prepolymer's ability to crosslink is particularly important and directly related to the number of photoreactive *o*MBA units per chain. The composition of the prepolymer was analyzed by ^{1}H-NMR spectroscopy (Figure 1B) and correlated with its molecular weight obtained from size exclusion chromatography (SEC; Figure 1C, described in detail in the Section 1.3.2, Supporting Information). The photoreactive *o*MBA units are evidenced by the resonances at 10.65 and 2.59 ppm, corresponding to the aldehyde and methyl protons of the *o*MBA unit, respectively. Furthermore, the presence of EHMA was confirmed by the resonance at 3.82 ppm, which is assigned to the oxymethylene unit of EHMA. The $\bar{M}_n$ of the prepolymer poly(PEMA-*co*-EHMA) was determined to be ≈15 400 Da ($Đ = 1.7$). As a result, the number of *o*MBA units per polymer chain was estimated to be close to 14. The incorporation ratio of EHMA and PEMA was determined by kinetic experiments.

To achieve a higher molar concentration of the photoreactive *o*MBA units for optimized quantum yields per polymer chain via the dimerization crosslinking reaction, the amount of solvent required to dissolve the prepolymer was minimized. Therefore, the glass transition temperature (T_g) of poly(PEMA-*co*-EHMA)

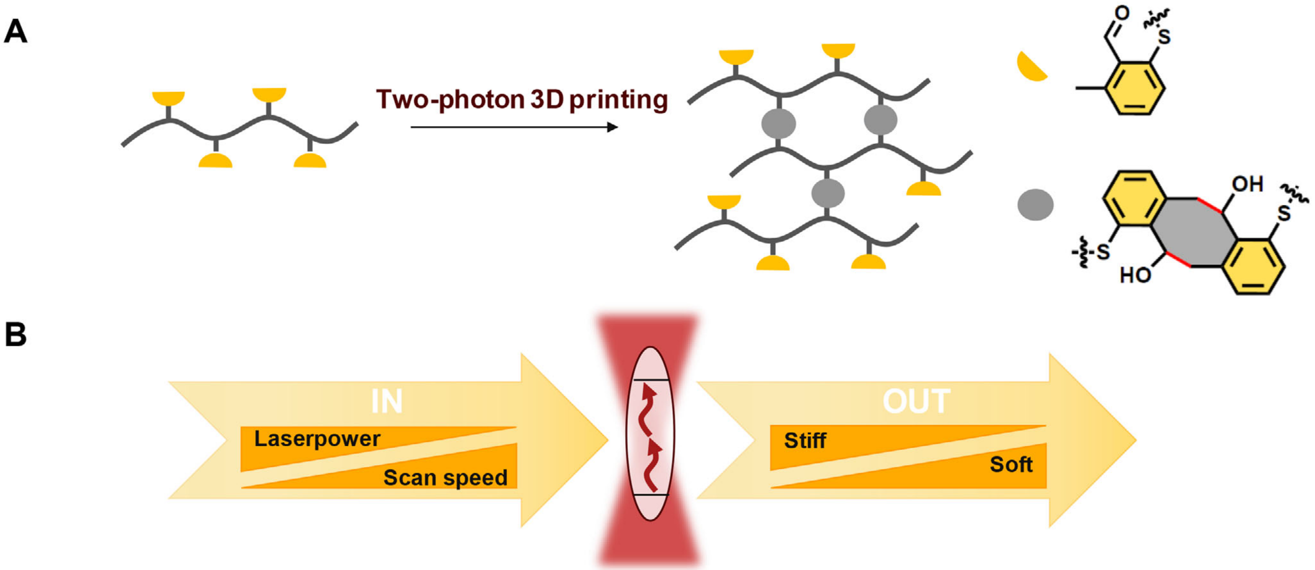

Scheme 1. A) Schematic and chemical representation of the resin's formulation and its crosslinking mechanism based on a step-growth process. B) The mechanical properties of the printed 3D microstructures are selected by carefully adjusting the printing parameters, i.e., laser power and scan speed.

was intentionally kept low by using the branched comonomer EHMA. A low T_g of the prepolymer at −10 °C was confirmed by differential scanning calorimetry (DSC, Figure S8, Supporting Information). An additional benefit of using EHMA is its ability to enhance the chain flexibility of the pre-polymer, and thereby facilitate the fabrication of soft materials.

The curing of the resin was tested using a 405 nm LED at varying irradiation times (Section 2.8, Supporting Information). Droplets of resin were cured, developed and the process steps were monitored via IR-spectroscopy. The consumption of the aldehyde unit present in the poly(PEMA-*co*-EHMA) and the formation of hydroxy groups in the cured network were observed as expected (Figures S24 and S25, Supporting Information, respectively). In addition, cured films were tested for the presence of extractable polymers or oligomers after development, i.e., after removal of uncured polymer and the solvent acetophenone (Table S6; Figure S26, Supporting Information). Since no significant reduction of weight of the films could be found upon leaching with THF solution, and no oligomeric species were detected in the leaching solution via SEC, it is expected that no migrating species are present in 2PP fabricated microstructures, which cannot be tested for leaching directly.

2.2. Printability Window

In 3D laser printing, the laser exposure dose (D_{exp}), which is governed by the combination of laser power and scan speed, is a key factor affecting the degree of crosslinking and thereby defining the boundary conditions of the printability window. If D_{exp} is above the polymerization threshold, printing can occur. However, crosslinking must not only lead to a crosslinked network beyond the gel point, but the generated crosslinks need to be sufficiently stable for the development step, consisting of immersion in toluene for 12 min, isopropanol for 2 min and critical point drying. In the development step, uncured resist including the solvent acetophenone is removed (refer to Section 2.3, Supporting Information). Furthermore, when D_{exp} exceeds a certain upper limit, microexplosions can occur due to resin heating upon intense and/or extended laser exposure and hence evaporation, preventing defect-free printing beyond that limit.

To identify the printability window of the resin, simple bridge structures were printed by systematically varying the laser power and scan speed for three ranges of scan speeds from slow to fast (slow, **Figure** 2A; medium Figure 2B; fast Figure 2C). For these samples, critical point drying (CPD) was applied to eliminate the capillary forces (C_F) effect, which mainly arises due to surface tension created during evaporation of the development solvent when drying under ambient conditions, often leading to collapse, shrinkage, or deformation of the 3D microstructure, especially in soft microstructures.[28] The optimal range of printing parameters for fabricating high resolution structures was identified through the comparison of scanning electron microscopy (SEM) images of the printed bridges (Figures S11–S14, Supporting Information). The printability window was determined as the set of conditions where the printed structure preserves its structural integrity and closely matches the design structure (displayed in green in Figure 2). Outside this window at a D_{exp}, which is still below or very close to the polymerization threshold, printing was either not possible at all or only possible with a lack of structural integrity (indicated by black and yellow, respectively, in Figure 2). The printability window of the resin is very large, starting at a low laser power of 3 mW and a scan speed of 20 µm s^{-1}, and extending to high laser power of 31% at a scan speed of 5000 µm s^{-1}. Beyond the printability window, the structures were still printable but with poor resolution due to overexposure (orange in Figure 2), or not printable at all due to microexplosions (red in Figure 2), arising from a higher D_{exp}. The effects of scan speed and laser power on microexplosions are clearly depicted in Figure 2. As the scan speed decreases, the microexplosions start to develop

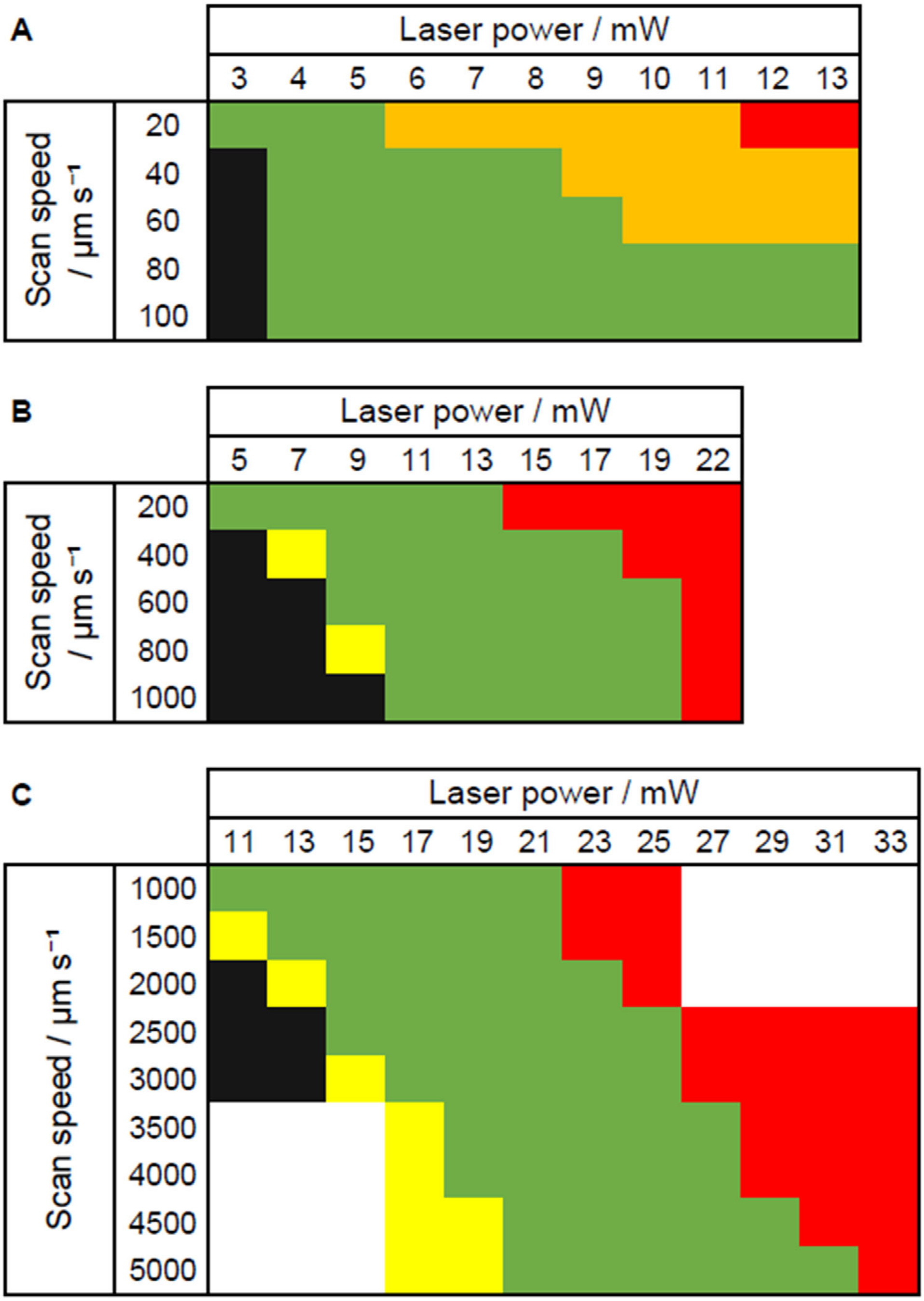

A

Scan speed / µm s^{-1}	3	4	5	6	7	8	9	10	11	12	13
20	🟩	🟩	🟩	🟧	🟧	🟧	🟧	🟧	🟧	🟥	🟥
40	⬛	🟩	🟩	🟩	🟩	🟩	🟧	🟧	🟧	🟧	🟧
60	⬛	🟩	🟩	🟩	🟩	🟩	🟩	🟧	🟧	🟧	🟧
80	⬛	🟩	🟩	🟩	🟩	🟩	🟩	🟩	🟩	🟩	🟩
100	⬛	🟩	🟩	🟩	🟩	🟩	🟩	🟩	🟩	🟩	🟩

Laser power / mW

B

Scan speed / µm s^{-1}	5	7	9	11	13	15	17	19	22
200	🟩	🟩	🟩	🟩	🟩	🟥	🟥	🟥	🟥
400	⬛	🟨	🟩	🟩	🟩	🟩	🟩	🟥	🟥
600	⬛	⬛	🟩	🟩	🟩	🟩	🟩	🟩	🟥
800	⬛	⬛	🟨	🟩	🟩	🟩	🟩	🟩	🟥
1000	⬛	⬛	⬛	🟩	🟩	🟩	🟩	🟩	🟥

Laser power / mW

C

Scan speed / µm s^{-1}	11	13	15	17	19	21	23	25	27	29	31	33
1000	🟩	🟩	🟩	🟩	🟩	🟩	🟥	🟥				
1500	🟨	🟩	🟩	🟩	🟩	🟩	🟥	🟥				
2000	⬛	🟨	🟩	🟩	🟩	🟩	🟩	🟥				
2500	⬛	⬛	🟩	🟩	🟩	🟩	🟩	🟩	🟥	🟥	🟥	🟥
3000	⬛	⬛	🟨	🟩	🟩	🟩	🟩	🟩	🟥	🟥	🟥	🟥
3500				🟨	🟩	🟩	🟩	🟩	🟩	🟥	🟥	🟥
4000				🟨	🟩	🟩	🟩	🟩	🟩	🟥	🟥	🟥
4500				🟨	🟨	🟩	🟩	🟩	🟩	🟩	🟥	🟥
5000				🟨	🟨	🟩	🟩	🟩	🟩	🟩	🟩	🟥

Laser power / mW

Figure 2. Printability window assessment of the resin within three different regions. A) scan speed range 20–100 µm s^{-1} and laser power range 3–13 mW, B) scan speed range 200–1000 µm s^{-1} and laser power range 5–22 mW, C) scan speed range 1000–5000 µm s^{-1} and laser power range 11–33 mW. Color code: black – not printable due to insufficient laser exposure dose ($\bar{D}_{exp}$), green – printable, yellow – printable but lacks structural integrity, orange – printable but with poor resolution, red – not printable.

at lower laser powers in comparison to the higher scan speeds due to a relatively long duration of laser exposure, resulting in higher heat dissipation. It is noteworthy that the printable laser power range at low laser powers broadens step-by-step, with each equal incremental increase of the scan speed, enabling printing in a broad laser power range at a constant scan speed (Figure 2).

Further, it is critical to note that the most consistent printing results were obtained using medium laser powers at each scan speed tested within the printability window, which represents the ideal region for printing, distant from the regions where under-exposure or overexposure can take place (Figure S15, Supporting Information).

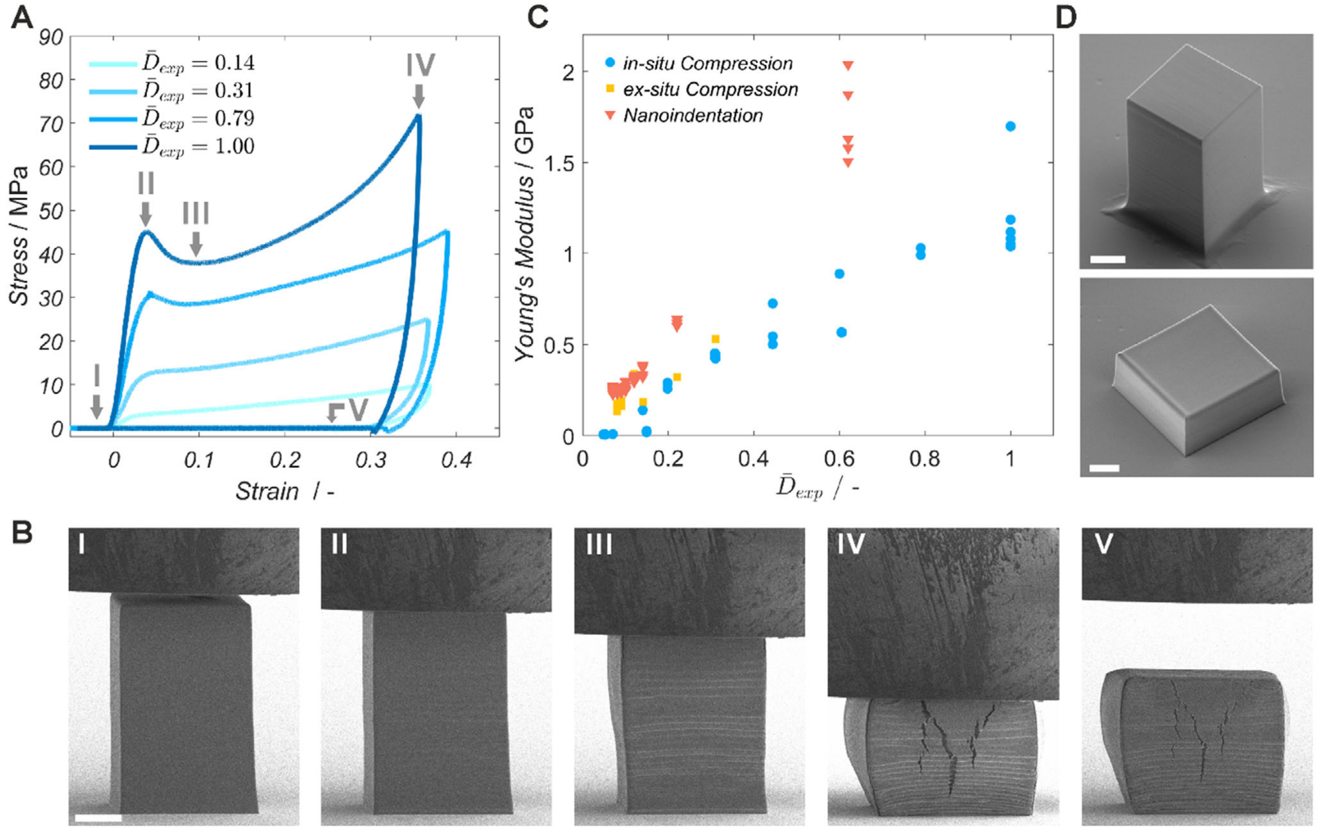

Figure 3. Range of the 2PLP-exposure-dose-control adjustable mechanical properties. A) In situ compression stress-strain curves of four representative micropillars with increasing relative exposure doses ($\bar{D}_{\text{exp}}$); B) corresponding in situ SEM still frames of $\bar{D}_{\text{exp}} = 1$ at the indicated stages of the curve in A; C) Young's moduli obtained from in situ and ex situ compressions as well as nanoindentation depending on $\bar{D}_{\text{exp}}$; D) representative ex situ compression (top) and nanoindentation (bottom) specimen prior to testing. Scale bars in B and D are 10 µm.

2.3. Mechanical Property Measurements

3D laser printing with varying exposure dose enabled our resin to afford a wide range of mechanical properties from rubbery soft to hard, with the adjustable Young's moduli (E) spanning more than two orders of magnitude from close to 10 MPa up to values above 1300 MPa. To establish the achievable range of mechanical properties depending on the delivered $\bar{D}_{exp}$, we used three distinct methods, in situ and ex situ micropillar compression and nanoindentation. Ex situ and in situ compression tests were employed utilizing a custom-made measurement setup and a Hysitron PI 89 Picoindenter (Bruker), respectively (refer to Section 2.5, Supporting Information). Nanoindentation tests were conducted via displacement-controlled continuous stiffness measurement (CSM), using a FT-NMT04 nanoindenter (Femto Tools, refer to Section 2.5, Supporting Information). Simple cuboid structures were printed for each method, using different printing parameters that are within the printing window. At each scan speed the laser power is adjusted such that it is positioned in the middle of the printability window since this region provided the most reproducible printing results. The mechanical properties of the printed 3D structures were subsequently analyzed. The Young's moduli were calculated from the initial linear elastic region of the compressive stress-strain curves, and from the CSM oscillatory signal of the indentation force-displacement curves (**Figure 3**; Figures S17A,B, S18, and S20; Tables S2, S3, and S5, Supporting Information). To compare the specimens taking into account both printing parameters at the same time, we report the measured properties as a function of the relative exposure dose ($\bar{D}_{exp}$), considering that $\bar{D}_{exp}$ is proportional to the square of intensity (∝ (laser power)^2) and exposure time (∝ (scan speed)$^{-1}$) (Equation 1, Tables S2, S3, and S5, Supporting Information).

$$D_{exp} \propto I^2 \, t_{exp} \tag{1}$$

Each specimen printed with a certain combination of scan speed and laser power, i.e., a certain set of PPs, is named unambiguously in Tables S1–S3 (Supporting Information), for instance "PP-9". The highest D_{exp} was achieved for PP-9 (laser power 9 mW, scan speed 50 µm s^{-1}) and was thus defined as 1. $\bar{D}_{exp}$ for other printing parameters was calculated relative to this value (Tables S1–S4, Supporting Information). All samples were measured after development.

In situ compression tests were performed with cuboid micropillars (cuboids with nominal dimensions of 38 µm in height and 20×20 µm^2 cross section) printed with $\bar{D}_{\text{exp}}$ values from 0.048 to 1. Figure 3A shows four representatives stress-strain curves for $\bar{D}_{\text{exp}}$ of 0.14 to 1 along with SEM still frames for $\bar{D}_{exp} = 1$ in Figure 3B. For $\bar{D}_{\text{exp}}$ of 0.14, the material exhibited a soft stress-strain behavior, as is characteristic for rubber-elastic polymers like PDMS.[29] After only a minimal initial linear elastic regime, the curve transitioned into an elongated stress plateau above 3% strain. The corresponding Young's modulus and yield strength were 140 MPa and 2.39 MPa, respectively. With increasing $\bar{D}_{\mathrm{exp}}$, the stress-strain responses steadily transitioned to a distinct, significantly stiffer and stronger, behavior, similar to previously reported 2PLP-printed thermosetting polymers (Figure 3C; Figure S18; Table S3, Supporting Information).[30] At the highest tested $\bar{D}_{\mathrm{exp}}$ of 1, the material showed a pronounced linear elastic region prior to the softening plateau with a nearly tenfold Young's modulus and yield strength of 1312 ± 341 MPa and 37.52 ± 0.21 MPa, respectively, compared to $\bar{D}_{\mathrm{exp}} = 0.14$. At the lowest tested $\bar{D}_{\mathrm{exp}} = 0.048$, we found a nearly 200-fold lower Young's modulus of 6.73 ± 1.04 MPa and a yield strength of 0.23 ± 0.10 MPa compared to $\bar{D}_{\mathrm{exp}} = 1$. All micropillars were observed to deform uniformly up to their yield point, followed by continuous bulging during the plateau stage up to the applied maximum strains of 36–39% (Figure 3B). Note that the observed horizontal wrinkling and vertical cracking may be considered an artefact confined to only the sputter coatings on the specimen surfaces. After unloading, residual strains ranged from 28% to 33%, indicating irreversible plastic deformation across all specimens with no significant trend with respect to $\bar{D}_{\mathrm{exp}}$.

To confirm the absolute values for these findings, ex situ compression tests were additionally performed using a custom-made mechanical property measurement setup in air atmosphere (Figure S16, Supporting Information). Here, 50 µm high cuboids with 30×30 µm^2 cross section were printed, varying the delivered $\bar{D}_{\mathrm{exp}}$ between 0.077 and 0.31. The mechanical property measurements demonstrate the same direct correlation between the laser exposure dose and Young's modulus found in previous tests (Figure 3C; Figure S17; Table S2, Supporting Information). The higher $\bar{D}_{\mathrm{exp}}$ is, the higher the Young's modulus becomes due to a higher degree of crosslinking (Figure 3; Table S2, Supporting Information). On the other hand, a reduction in $\bar{D}_{exp}$ generates networks with lower degrees of crosslinking,[31] thus allowing for the production of softer materials (Figure 3; Table S2, Supporting Information). For instance PP-1 ($\bar{D}_{\mathrm{exp}} = 0.31$, laser power 5 mW, scan speed 50 µm s^{-1}) and PP-7 ($\bar{D}_{\mathrm{exp}} = 0.078$, laser power 21 mW, scan speed 3500 µm s^{-1}), led to fabrication of stiffer (Young's modulus: 531 ± 35.33 MPa) and softer (Young's modulus: 135 ± 6.96 MPa) materials, respectively (Figure 3; Table S2, Supporting Information).

Additionally, displacement-controlled continuous stiffness (CSM) nanoindentation tests were conducted on 2PLP-printed pads with $\bar{D}_{exp}$ values ranging from 0.071 to 0.62 (Figure 3C; Figure S20; Table S5, Supporting Information). Up to $\bar{D}_{\mathrm{exp}}$ of 0.089, the determined Young's moduli fell within the narrow range of 241–274 MPa. As the $\bar{D}_{\mathrm{exp}}$ increased, the Young's moduli steadily increased to 1724 ± 199 MPa for the highest tested $\bar{D}_{\mathrm{exp}}$ of 0.62, marking an approximately sevenfold modulus increase in the $\bar{D}_{\mathrm{exp}}$-range from 0.071 to 0.62. The hardness followed a comparable trend. The found values are in agreement with the data from the in situ compression experiments (Tables S3 and S4, Supporting Information).

On the basis of the mechanical property measurements performed using three independent measurement methods, it is confirmed that by merely adjusting the printing parameters, the prepolymer resin is capable of fabricating 3D microstructures with an exceptionally wide range of material properties with Young's moduli spanning more than two orders of magnitude. In comparison, all three of our mechanical datasets show good correlation, having independently identified matching Young's modulus spans and trends for a given $\bar{D}_{\mathrm{exp}}$ range (Figure 3C). Within the pillar compressions, the in situ and ex situ results agree well, suggesting the properties of our material are insensitive to atmospheric conditions such as humidity. Expectedly, the micropillar compression data are shifted to lower values with respect to the nanoindentation results. While providing the advantage of capturing the full stress-strain behavior, slight tip-sample misalignment commonly leads to underestimation of Young's modulus in pillar compression. With near-ideal alignment, pillar compression-measured moduli may be expected to approach nanoindentation results. Conversely, nanoindentation may overestimate the Young's moduli of soft polymers in the presence of adhesion related pull-in effects that complicate identification of the tip contact point,[32] however, no such effects were observed in our data (Figure S20A,B, Supporting Information). In addition, we have investigated the storage stability of the printed specimen and found a decrease in Young's modulus by a factor of ≈2 after five months of storage (Figure S19; Table S5, Supporting Information).

2.4. Complex 3D Microstructure Printing

We have demonstrated above that the prepolymer resin exhibits excellent printability over a broad range of laser powers and scan speeds. To further assess the printing quality in terms of resolution, complex 3D microstructures such as Benchy and Bucky-ball structures were printed, especially using the printing parameters from which soft (PP-6: laser power 19 mW, scan speed 2500 µm s^{-1}) and stiff (PP-2: laser power 13 mW, scan speed 500 µm s^{-1}) materials are obtained. All the fine details of the Benchy and Bucky-ball structures can be printed and are very well-defined using the conditions for the stiff material (**Figure** 4A,B) as well as the conditions for the soft material (Figure 4C,D). It is noteworthy that the difference in dimensions stems from the variable shrinkage behavior of the resin at different printing conditions leading to varying crosslinking density. We also observed the lateral shrinkage behavior of the specimen printed for mechanical property measurements, refer to Table S7 (Supporting Information). In summary, moderate shrinkage up to 8% was observed. The close-up SEM images of each Benchy with different dimensions and Bucky-balls, printed at selected conditions (PP-2, PP-4, PP-6), are provided in detail in Figures S21 and S22 (Supporting Information).

2.5. Visualization of Mechanical Property Differences

To visually demonstrate the differences in mechanical properties of stiff and soft materials from the same prepolymer resin, an experiment was performed in which the tendency of the different materials to deform under capillary forces (F_c) was evaluated. Even though deformation is typically undesirable and mitigated using CPD to obtain free-standing structures after

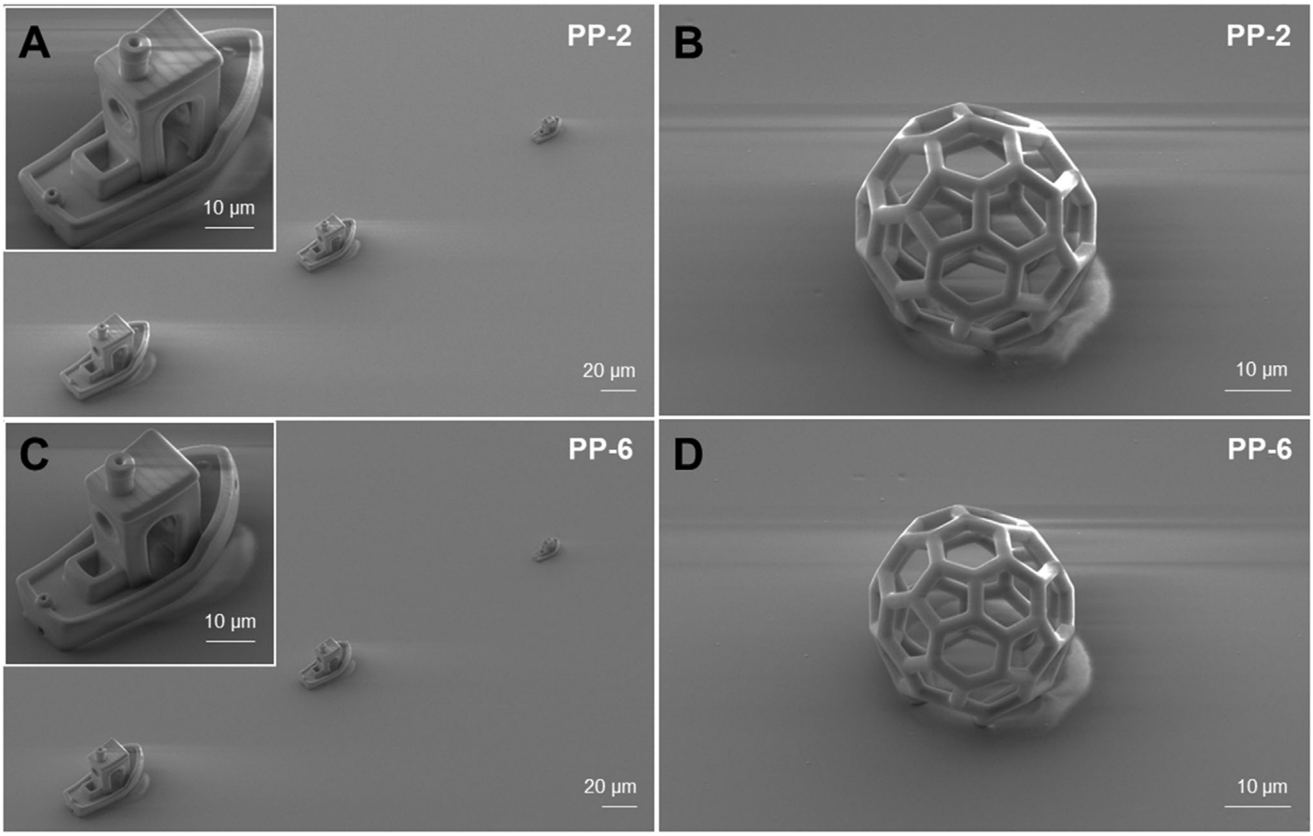

Figure 4. SEM images of (A, C) Benchy and (B, D) Bucky-ball structures printed at the corresponding printing parameters; PP-2: laser power 13 mW, scan speed 500 µm s^{-1}, PP-6: laser power 19 mW, scan speed 2500 µm s^{-1}.

development,[33] here it is intentionally employed as an external compressive stress, under which the reaction of stiff and soft materials was investigated. Initially, two arrays of stiff and soft micropillars were printed with printing parameters PP-2 and PP-6, respectively, and developed and dried using CPD to maintain their structural integrity at first. Subsequently, a droplet of isopropanol was added onto the critical point dried 3D micropillars and allowed to evaporate under ambient conditions, effectively exposing the sample to F_c. The reaction that the 3D micropillars gave in response to F_c was monitored using light microscopy (refer to Section 2.7; Figure S23 and Video S1, Supporting Information), and SEM images were recorded before and after F_c exposure. Both stiff and soft micropillars retained their structural integrity upon CPD and prior to F_c impact (**Figure 5A,B**). Upon exposure to F_c during air-drying, the stiff micropillars remained upright, resisting this external force (Figure 5C), while an immediate collapse of the softest micropillars was observed (Figure 5D). The lower crosslinking density of the soft materials made them more susceptible to F_c-induced deformation compared to the stiff materials. The SEM images taken after F_c exposure clearly depict that the pillars remained intact and attached to the substrate, confirming that solely the softness of the resist was responsible for the bending of the structures.

2.6. Multi-Material 3D Structures

The ability to adjust a wide range of mechanical properties enables our photoresin to print multi-material structures in a single-step process via simple gray-tone control of the applied printing parameters, eliminating the need for sequential print-develop-print procedures[34] or microfluidics-integrations,[35] as required by previously reported multi-material 2PLP approaches. In the following, three multi-material structures are demonstrated, manufactured from our material via single-step gray-tone 2PLP. They demonstrate unique mechanical responses and properties that are inaccessible within single-material designs. While our study focuses on causing large and abrupt changes in material properties despite varying shrinkage behavior, the material could also be utilized for stiffness gradients by changing the properties incrementally and in a faster sequence.

Figure 6A visualizes the span of adjustable mechanical properties in a compression experiment with a multi-material micropillar, where a soft layer was sandwiched between two approximately one order of magnitude stiffer blocks. The soft layer, printed with 30% $\bar{D}_{\mathrm{exp}}$ relative to the hard blocks, was angled at 45° with respect to the horizontal plane, corresponding to the maximum shear stress orientation under vertical load. Thus, the multi-material design converts an applied uniaxial compression into a

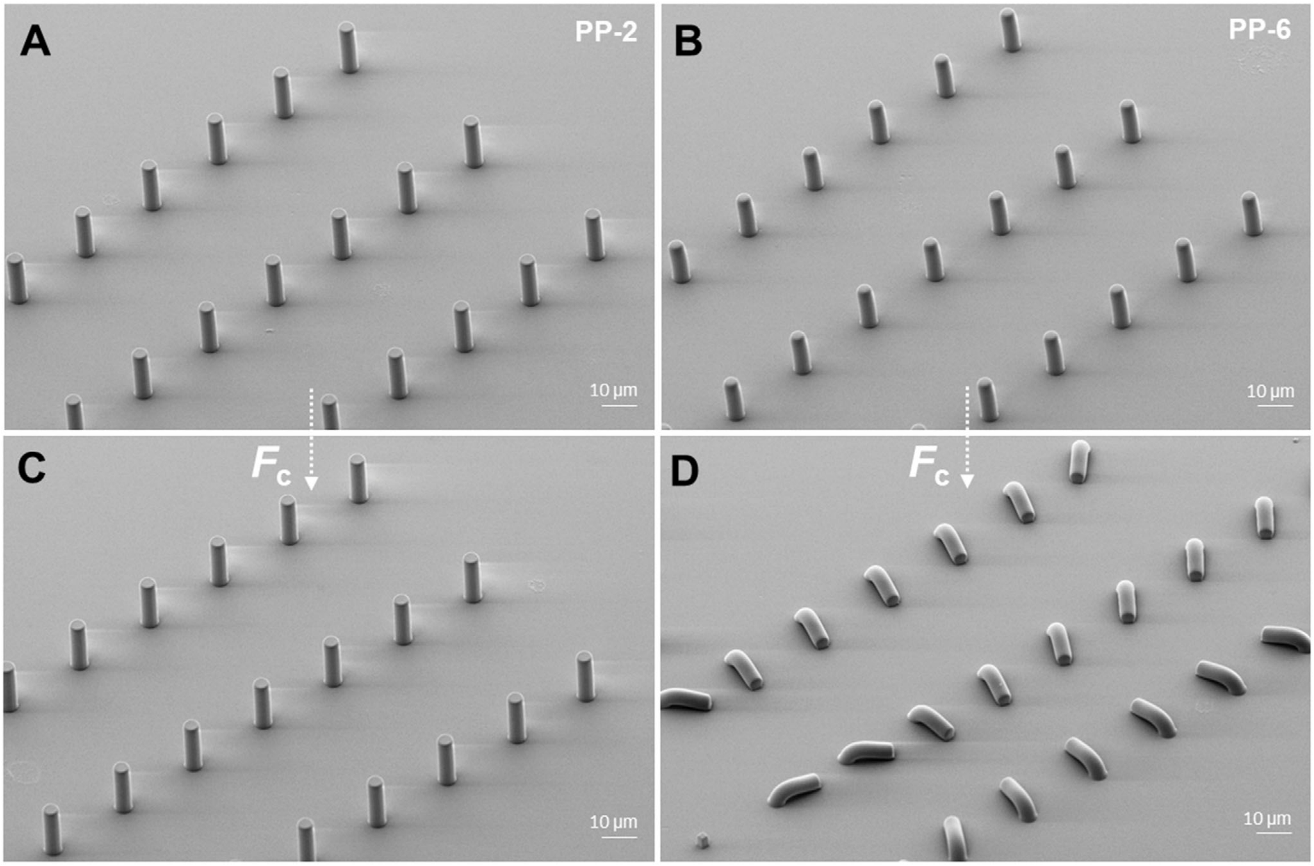

Figure 5. SEM images of the stiffest and softest micropillars printed using the respective parameters PP-2 and PP-6, (A,B) before and (C,D) after exposure to capillary forces.

shear deformation of the soft layer (refer to Video S2, Supporting Information). Initially, the deformation of both the soft and hard components was largely elastic, with a linearly increasing stress-strain response. Coinciding with the yield point at ≈ 0.6 µm displacement, corresponding to ≈1% axial strain, the deformation pattern started to localize via the formation of a pronounced shear band confined to the soft phase of the specimen (Figure 6A-II). With the shear stress (τ) given by $\tau = F/(2A)\sin(2\theta)$, where F is the applied force and A the pillar cross-sectional area, the shear stress at yield in the soft layer, oriented at the angle $\theta = 45°$ was 0.3 MPa. With continued loading, the shear deformation steadily increased further. Simultaneously, the stiff top and bottom blocks were not observed to undergo notable inelastic deformation up to the applied maximum axial strain of 12% at 6.6 µm displacement (Figure 6A-III). At this point, the applied load corresponded to a maximum shear stress of 1.2 MPa, leaving the soft layer severely deformed. Meanwhile, the interface between the two materials appeared fully intact, indicating a bonding strength between the two phases at least four times stronger than the yield strength of the softer bonding partner. Observable surface wrinkling and cracking are considered artifacts limited to the sputter coating applied for SEM imaging. After unloading, the soft layer exhibited notable permanent deformation, while the stiff blocks remained intact (Figure 6A-IV). Compared to the homogenous structures in Figure 3A,B, this soft-stiff hybrid clearly exhibits a distinct deformation behavior and corresponding mechanical properties.

Figure 6B shows a chiral architecture, which achieves rotatory motion under an applied compression by a bi-material beam design. The structure is constructed from four radially patterned vertical beams, each divided into a soft and stiff half along their length. Two stiff horizontal plates at the top and bottom connect the beams via flexible soft hinges, a third one intersects the beams at their half-length. Due to the bi-material layout, the beams' deformation behavior is programmed to always buckle toward the hard side under axial compression. When arranged in the chosen rotational symmetric pattern, this facilitates a counterclockwise rotation motion of the structure's middle plate (from the top view, refer to Video S3, Supporting Information). The soft and hard materials were printed with the same material properties as in the previous example. Upon loading, the architecture first displayed a linear-elastic behavior, until a displacement of 5.2 µm, where the bi-material beams started to unanimously buckle in the expected direction, initiating the rotation of the middle plate (Figure 6B-II). After a peak load of 4.55 mN, the structure showed characteristic post-buckling softening with negative stiffness (Figure 6B-III). The load was released before any significant structural damage occurred, reaching a maximum displacement of 9.5 µm, which corresponded to a rotation of the middle plate by ≈23°.

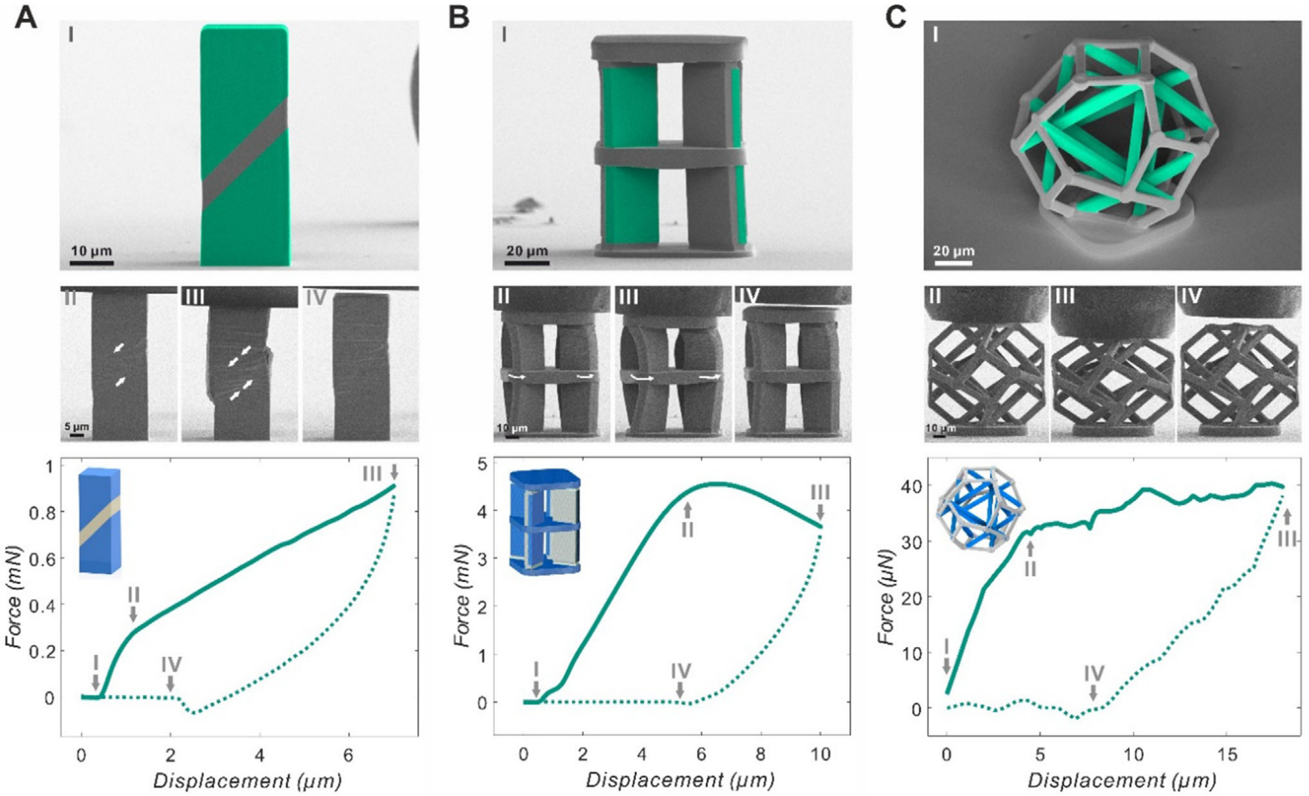

Figure 6. Multi-material demonstrator structures and their mechanical behavior under uniaxial compression. The stiff and soft phases were printed with printing parameters PP-1 and PP-5, respectively, resulting in nearly threefold differing Young's moduli, with a lower value of ≈162 MPa. A) Multi-material micropillar with a 45° soft middle layer; B) Chiral bi-material beam structure that transforms an applied compression into twisting. C) Truncated octahedron tensegrity metamaterial cell comprised of a continuous soft cable network and isolated stiff bars. Force-displacement curves are provided, along with SEM images showing the deformation at the indicated stages. In A-I, B-I and C-I the stiff blocks, bi-material beams and compression bars, respectively, are colorized in green.

Figure 6C depicts a tensegrity metamaterial cell, successfully expanding our gray-tone multi-material approach toward highly intricate 3D geometries. Tensegrities are a unique type of truss structure, comprised of a continuous network of tensile elements, which connects compression members that are isolated from one another. Multi-material tensegrities from elastic tensile cables and rigid struts, such as for soft robotics,[36] enable programming of a wide range of flexible non-linear large-strain deformations while retaining high stiffness-to-mass ratios. Here we take this approach to the microscale, adopting a design,[37] which has been exploited in damage-resistant metamaterials.[38] The truncated octahedron cell was printed from a soft tensile network along the surface edges and stiff isolated compression struts located within the structure. Again, the printing parameters were identical to the previous examples. When subjected to uniaxial compression, the tensegrity cell initially exhibited largely uniform deformation (Figure 6C-II), with a linear-elastic force-displacement region (refer to Video S4, Supporting Information). At ≈5 µm displacement (≈5.2% strain), the response shifted to a near-constant maximum force plateau, which was maintained until the applied maximum displacement of 18 µm (≈19% strain). Large-strain elastic-ideal plastic behavior is typically challenging to achieve and irreversible in conventional truss-lattice materials. Here, the measured response was primarily an elastic and reversible mechanism, with the majority of the deformation occurring in the plateau stage (Figure 6C-II & III) via hinging and stretching of the soft cables, while only limited deformation of the hard struts was observed.

3. Conclusion

We introduce a prepolymer containing pendant *o*MBA units as the sole constituent of a resin formulation without any crosslinker or photoinitiator for the fabrication of 3D microstructures with strongly varying mechanical properties via 2PLP. By employing a gray-tone lithography approach, we locally control the material properties in a single production step by simply adjusting the printing parameters (i.e., laser power, scan speed). A clear correlation between the relative $\bar{D}_{exp}$ and degree of crosslinking and thereby mechanical properties was identified. On the one hand, stiff materials with a Young's modulus above 1300 MPa can be fabricated, using a higher $\bar{D}_{exp}$, resulting from a higher degree of crosslinking. On the other hand, soft materials with a Young's modulus of lower than 10 MPa can be produced utilizing a lower $\bar{D}_{exp}$, achieving a lower degree of crosslinking while maintaining structural integrity of printed objects. These results represent a bandwidth of Young's moduli of two orders of magnitude between the stiffest and softest materials, providing an unprecedentedly broad range of material properties using a single resin formulation. The introduced broad material property window will be highly beneficial for applications requiring diverse mechanical properties, such as biological applications, microfluidics, or soft robotics.[13a]

Supporting Information

Supporting Information is available from the Wiley Online Library or from the author.

Acknowledgements

T.N.E. and J.L. contributed equally to this work. C.B.-K. and M.W. acknowledge key funding by the Deutsche Forschungsgemeinschaft (DFG, German Research Foundation) under Germany's Excellence Strategy for the Excellence Cluster "3D Matter Made to Order" (EXC-2082/1-390761711), by the Carl Zeiss Foundation, and by the Helmholtz program "Materials Systems Engineering". C.B.-K. further acknowledges funding from the Australian Research Council (ARC) in the form of a Laureate Fellowship (FL170100014), enabling his photochemical research as well as continued key support from the Queensland University of Technology (QUT). J.B. acknowledges funding from the Deutsche Forschungsgemeinschaft (DFG, German Research Foundation) (grant BA 5778/2-1). The authors are grateful to F. Ganslmaier and Dr. B. Weinert for ESI-MS measurements. Open Access publishing facilitated by Queensland University of Technology, as part of the Wiley – Queensland University of Technology agreement via the Council of Australian University Librarians.

Conflict of Interest

The authors declare no conflict of interest.

Data Availability Statement

The data that support the findings of this study are available in the supplementary material of this article.

Keywords

gray-tone lithography, mechanical property tuning, PDMS like soft materials, two-photon 3D multi-material printing

Received: May 6, 2025
Revised: June 24, 2025
Published online:

---

[1] a) W. Gao, H. Chao, Y.-C. Zheng, W.-C. Zhang, J. Liu, F. Jin, X.-Z. Dong, Y.-H. Liu, S.-J. Li, M.-L. Zheng, *ACS Appl. Mater. Interfaces* **2021**, *13*, 27796; b) J. K. Gansel, M. Thiel, M. S. Rill, M. Decker, K. Bade, V. Saile, G. von Freymann, S. Linden, M. Wegener, *Science* **2009**, *325*, 1513; c) M. Carlotti, V. Mattoli, *Small* **2019**, *15*, 1902687; d) F. Jin, J. Liu, Y.-Y. Zhao, X.-Z. Dong, M.-L. Zheng, X.-M. Duan, *Nat. Commun.* **2022**, *13*, 1357; e) M. Carlotti, O. Tricinci, V. Mattoli, *Adv. Mater. Technol.* **2022**, *7*, 2101590.

[2] a) J. Fischer, M. Wegener, *Laser Photonics Rev.* **2013**, *7*, 22; b) K.-S. Lee, R. H. Kim, D.-Y. Yang, S. H. Park, *Prog. Polym. Sci.* **2008**, *33*, 631.

[3] a) I. Sakellari, E. Kabouraki, D. Gray, V. Purlys, C. Fotakis, A. Pikulin, N. Bityurin, M. Vamvakaki, M. Farsari, *ACS Nano* **2012**, *6*, 2302; b) S. Kawata, H.-B. Sun, T. Tanaka, K. Takada, *Nature* **2001**, *412*, 697; c) J. K. Hohmann, M. Renner, E. H. Waller, G. von Freymann, *Adv. Opt. Mater.* **2015**, *3*, 1488.

[4] L. Yang, H. Hu, A. Scholz, F. Feist, G. Cadilha Marques, S. Kraus, N. M. Bojanowski, E. Blasco, C. Barner-Kowollik, J. Aghassi-Hagmann, M. Wegener, *Nat. Commun.* **2023**, *14*, 1103.

[5] S. I. Rich, R. J. Wood, C. Majidi, *Nat. Electron.* **2018**, *1*, 102.

[6] B.-B. Xu, Y.-L. Zhang, H. Xia, W.-F. Dong, H. Ding, H.-B. Sun, *Lab Chip* **2013**, *13*, 1677.

[7] a) B. Richter, V. Hahn, S. Bertels, T. K. Claus, M. Wegener, G. Delaittre, C. Barner-Kowollik, M. Bastmeyer, *Adv. Mater.* **2017**, *29*, 1604342; b) N. Munding, M. Fladung, Y. Chen, M. Hippler, A. D. Ho, M. Wegener, M. Bastmeyer, M. Tanaka, *Adv. Funct. Mater.* **2024**, *34*, 2301133.

[8] a) L. Sun, H. Ni, X. Liu, D. Zhang, Y. Zeng, X. Han, L. Jiang, H. Chen, X. Zhao, Z. Gu, *ACS Photonics* **2018**, *5*, 4872; b) T. Gissibl, S. Thiele, A. Herkommer, H. Giessen, *Nat. Photonics* **2016**, *10*, 554.

[9] a) J. Qu, M. Kadic, A. Naber, M. Wegener, *Sci. Rep.* **2017**, *7*, 40643; b) M. Hippler, E. Blasco, J. Qu, M. Tanaka, C. Barner-Kowollik, M. Wegener, M. Bastmeyer, *Nat. Commun.* **2019**, *10*, 232; c) L. Yang, F. Mayer, U. H. F. Bunz, E. Blasco, M. Wegener, *Light Adv. Manuf.* **2021**, *2*, 296.

[10] K. Ehrmann, C. Barner-Kowollik, *J. Am. Chem. Soc.* **2023**, *145*, 24438.

[11] a) B. Kaehr, J. B. Shear, *Science* **2008**, *105*, 8850; b) S. C. Gauci, K. Ehrmann, M. Gernhardt, B. Tuten, E. Blasco, H. Frisch, V. Jayalatharachchi, J. P. Blinco, H. A. Houck, C. Barner-Kowollik, *Adv. Mater.* **2023**, *35*, 2300151; c) X. Kuang, J. Wu, K. Chen, Z. Zhao, Z. Ding, F. Hu, D. Fang, H. J. Qi, *Sci. Adv.* **2019**, *5*, aav5790.

[12] a) E. D. Lemma, F. Rizzi, T. Dattoma, B. Spagnolo, L. Sileo, A. Qualtieri, M. De Vittorio, F. Pisanello, *IEEE Trans. Nanotechnol.* **2016**, *16*, 23; b) P. F. van Altena, A. Accardo, *Polymers* **2023**, *15*, 1816; c) M. Belqat, X. Wu, L. P. C. Gomez, J.-P. Malval, S. Dominici, B. Leuschel, A. Spangenberg, K. Mougin, *Addit. Manuf.* **2021**, *47*, 102232; d) X. Gou, M. Zheng, Y. Zhao, X. Dong, F. Jin, J. Xing, X. Duan, *Appl. Surf. Sci.* **2017**, *416*, 273.

[13] a) Y. Jia, C. A. Spiegel, A. Welle, S. Heißler, E. Sedghamiz, M. Liu, W. Wenzel, M. Hackner, J. P. Spatz, M. Tsotsalas, *Adv. Funct. Mater.* **2023**, *33*, 2207826; b) M. Gernhardt, E. Blasco, M. Hippler, J. Blinco, M. Bastmeyer, M. Wegener, H. Frisch, C. Barner-Kowollik, *Adv. Mater.* **2019**, *31*, 1901269.

[14] A. Acuña, W. Adam, F. Amat, D. Armesto, T. Atvars, A. Bard, E. Bill, L. Björn, C. Bohne, J. Bolton, *Pure Appl. Chem.* **2007**, *79*, 293.

[15] a) M. W. Tibbitt, A. M. Kloxin, L. A. Sawicki, K. S. Anseth, *Macromolecules* **2013**, *46*, 2785; b) S. Lin-Gibson, R. L. Jones, N. R. Washburn, F. Horkay, *Macromolecules* **2005**, *38*, 2897.

[16] a) M. Ahmadi, K. Ehrmann, T. Koch, R. Liska, J. r. Stampfl, *Chem. Rev.* **2024**, *124*, 3978; b) Y. Gu, J. Zhao, J. A. Johnson, *Trends Chem.* **2019**, *1*, 318; c) F. Di Lorenzo, S. Seiffert, *Polym. Chem.* **2015**, *6*, 5515; d) J. Wu, Z. Zhao, C. M. Hamel, X. Mu, X. Kuang, Z. Guo, H. J. Qi, *J. Mech. Phys. Solids* **2018**, *112*, 25; e) K. Ashikaga, S. Ito, M. Yamamoto, Y. Nishijima, *Polym. J.* **1987**, *19*, 727; f) B. D. Fairbanks, L. J. Macdougall, S. Mavila, J. Sinha, B. E. Kirkpatrick, K. S. Anseth, C. N. Bowman, *Chem. Rev.* **2021**, *121*, 6915.

[17] a) J. Torgersen, X. H. Qin, Z. Li, A. Ovsianikov, R. Liska, J. Stampfl, *Adv. Funct. Mater.* **2013**, *23*, 4542; b) P. E. Petrochenko, J. Torgersen, P. Gruber, L. A. Hicks, J. Zheng, G. Kumar, R. J. Narayan, P. L. Goering, R. Liska, J. Stampfl, *Adv. Healthcare Mater.* **2015**, *4*, 739; c) J.-F. Xing, M.-L. Zheng, X.-M. Duan, *Chem. Soc. Rev.* **2015**, *44*, 5031.

[18] C. A. Coenjarts, C. K. Ober, *Chem. Mater.* **2004**, *16*, 5556.

[19] J. J. Schwartz, *MRS Bulletin* **2022**, *47*, 628.

[20] T. Sakai, T. Matsunaga, Y. Yamamoto, C. Ito, R. Yoshida, S. Suzuki, N. Sasaki, M. Shibayama, U.-I. Chung, *Macromolecules* **2008**, *41*, 5379.

[21] G. S. Kumar, Q. Lin, *Chem. Rev.* **2020**, *121*, 6991.

[22] G. Yilmaz, Y. Yagci, *Prog. Polym. Sci.* **2020**, *100*, 101178.

[23] A. Bagheri, J. Jin, *ACS. Appl. Polym. Mater.* **2019**, *1*, 593.
[24] a) S. C. Gauci, M. Gernhardt, H. Frisch, H. A. Houck, J. P. Blinco, E. Blasco, B. T. Tuten, C. Barner-Kowollik, *Adv. Funct. Mater.* **2023**, *33*, 2206303; b) A. S. Quick, H. Rothfuss, A. Welle, B. Richter, J. Fischer, M. Wegener, C. Barner-Kowollik, *Adv. Funct. Mater.* **2014**, *24*, 3571.
[25] J. P. Hooker, F. Feist, L. Delafresnaye, L. Barner, C. Barner-Kowollik, *Adv. Funct. Mater.* **2020**, *30*, 1905399.
[26] F. Feist, J. P. Menzel, T. Weil, J. P. Blinco, C. Barner-Kowollik, *J. Am. Chem. Soc.* **2018**, *140*, 11848.
[27] T. Furuncuoglu, I. Ugur, I. Degirmenci, V. Aviyente, *Macromolecules* **2010**, *43*, 1823.
[28] J. Purtov, A. Verch, P. Rogin, R. Hensel, *Microelectron. Eng.* **2018**, *194*, 45.
[29] T. K. Kim, J. K. Kim, O. C. Jeong, *Microelectron. Eng.* **2011**, *88*, 1982.
[30] J. Bauer, A. Guell Izard, Y. Zhang, T. Baldacchini, L. Valdevit, *Adv. Mater. Technol.* **2019**, *4*, 1900146.
[31] S. O. Catt, M. Hackner, J. P. Spatz, E. Blasco, *Small* **2023**, *19*, 2300844.
[32] a) Z. Wang, A. A. Volinsky, N. D. Gallant, *J. Appl. Polym. Sci.* **2015**, *132*, 41384; b) J. K. Deuschle, E. J. d. Souza, E. Arzt, S. Enders, *Int. J. Mater. Res.* **2010**, *101*, 1014.
[33] H. Namatsu, K. Yamazaki, K. Kurihara, *Microelectron. Eng.* **1999**, *46*, 129.
[34] E. Wdowiak, M. Ziemczonok, J. Martinez-Carranza, A. Kuś, *Addit. Manuf.* **2023**, *73*, 103666.
[35] a) F. Mayer, S. Richter, J. Westhauser, E. Blasco, C. Barner-Kowollik, M. Wegener, *Sci. Adv.* **2019**, *5*, aau9160; b) A. C. Lamont, M. A. Restaino, M. J. Kim, R. D. Sochol, *Lab Chip* **2019**, *19*, 2340.
[36] H. Lee, Y. Jang, J. K. Choe, S. Lee, H. Song, J. P. Lee, N. Lone, J. Kim, *Sci. Robot.* **2020**, *5*, aay9024.
[37] J. J. Rimoli, R. K. Pal, *Composites, Part B* **2017**, *115*, 30.
[38] J. Bauer, J. A. Kraus, C. Crook, J. J. Rimoli, L. Valdevit, *Adv. Mater.* **2021**, *33*, 2005647.